nanoPhos enables ultra-sensitive and cell-type resolved spatial phosphoproteomics

Denys Oliinyk[1*], Tim Heymann[1*], Lukas Henneberg[1], Anastasiya Bardziukova[1], Marvin Thielert[1], Jeppe Kjærgaard[2], Sabine Vasconez[1], Marc Oeller[1], Edwin H. Rodriguez[1], Florian A. Rosenberger[1,3] and Matthias Mann[1]

[1]*Department of Proteomics and Signal Transduction, Max Planck Institute of Biochemistry, Martinsried, Germany*

[2]*NNF Center for Basic Metabolic Research, University of Copenhagen, Copenhagen, Denmark*

[3]*Department of Medical Biochemistry and Biophysics, Karolinska Institutet, Solna, Sweden*

[*]*These authors contributed equally*

Abstract

Mass spectrometry (MS)-based phosphoproteomics has transformed our understanding of cell signaling, yet current workflows face limitations in sensitivity and spatial resolution when applied to sub-microgram scale protein inputs. Here, we present nanoPhos, a robust method for ultra-sensitive phosphoproteomics, which allows deep coverage at high throughput and is compatible with Deep Visual Proteomics (DVP). It employs loss-less solid phase extraction capture (SPEC) for sample preparation and protein processing, followed by automated zero-volume phosphopeptide enrichment using Fe(III)-NTA cartridges. nanoPhos identifies over 55,000 unique phosphorylation sites from 1 µg cell lysate and over 8,000 from as little as 10 ng, a hundred-fold more identifications than recent protocols. In combination with laser microdissection, it enables cell-type and anatomically resolved phosphoproteomics of mouse brain tissue with spatial fidelity and depth of more than 17,000 phosphosites from only 1000 cell shapes. This establishes nanoPhos as a versatile and ultra-sensitive platform for probing cell types dispersed in heterogenous tissue and extends DVP to post-translational modifications.

Introduction

Modern MS-based phosphoproteomics has become a powerful tool for mapping signaling networks at proteome scale[1,2]. Over the past decade, major advances in MS instrumentation, sample preparation and data analysis have enabled increasingly deep and quantitative analysis of protein phosphorylation from diminishing input quantities (from milligrams of input material to the microgram range[3–5]). Significant contributions to this evolution were streamlined workflows such as EasyPhos, which minimized manual sample processing and enabled high-throughput phosphoproteome profiling, thereby opening up large-scale biological applications[6–10]. More recently, the µPhos platform extended these capabilities to sub-milligram or low-microgram inputs by efficiently optimizing phosphopeptide enrichment in 96-well plate formats[11]. These efforts enabled the in-depth mapping of phosphorylation networks in cells and tissues and their functional characterization in multi-condition perturbation studies and drug profiling[12]

However, several key challenges have prevented the further miniaturization of phosphoproteomics workflows towards nanogram-scale protein input amounts. These include continued reliance on relatively large processing volumes in the phosphopeptide enrichment step due to the necessity to maintain optimal peptide concentrations for bead-based enrichment and high percentages of acetonitrile. Furthermore, the presence of various detergents during phosphopeptide enrichment, while important for cell lysis, decreases its efficiency[13]. Such technical aspects have limited the sensitivity of phosphoproteomics workflows. Addressing these challenges could achieve the next-generation sensitivity needed to extend phosphoproteomics to a cell type-resolved and spatial contexts.

We recently developed Deep Visual Proteomics (DVP), a spatially resolved proteomics approach that combines high-content imaging, AI-driven cell classification, and laser microdissection with ultra-sensitive mass spectrometry to profile proteomes at single-cell type resolution[14]. So far, DVP has been limited to protein measurements only. Extending it to study cell signaling would open a new biological dimension - revealing how signaling networks operate within their native spatial and cellular context[15–18]. Here we describe nanoPhos, a streamlined phosphoproteomics workflow that addresses inherent challenges in phosphoproteomics sample preparation and allows for processing of nanogram input. Application of nanoPhos to cells in culture, EGF-stimulated cells, and

tissue sections (DVP) enables deep, cell-type resolved, and spatial phosphoproteomics data., capturing signal transduction *in vivo*.

Results

A phosphoproteomics workflow for nanogram-scale samples

The core principle of nanoPhos is the integration of detergent-based lysis with our recently developed Solid-Phase Extraction and Capture (SPEC) tip-based protein processing workflow (Heymann, Oliinyk, Henneberg et. al, in preparation) (**Fig. 1**). SPEC concentrates proteins into nanoliter-scale volumes within a single pipette tip, enabling efficient digestion with fast kinetics and broad detergent compatibility. This allows strong lysis conditions to be used without the sample losses typically associated with detergent removal. As phosphorylation is a somewhat labile PTM, we routinely use 2% SDC in nanoPhos, ensuring that phosphatase activity is effectively quenched and phosphosites can be analyzed even on insoluble proteins. Peptides are eluted in low volume and directly subjected to zero-dead-volume phosphopeptide enrichment on a robotic platform (AssayMAP Bravo), using Fe(III)-NTA cartridges. We found that each module - lysis, digestion, enrichment - can be independently optimized and suited to the users' needs, thus maintaining full compatibility with high-throughput formats and ultra-low input amounts (Methods).

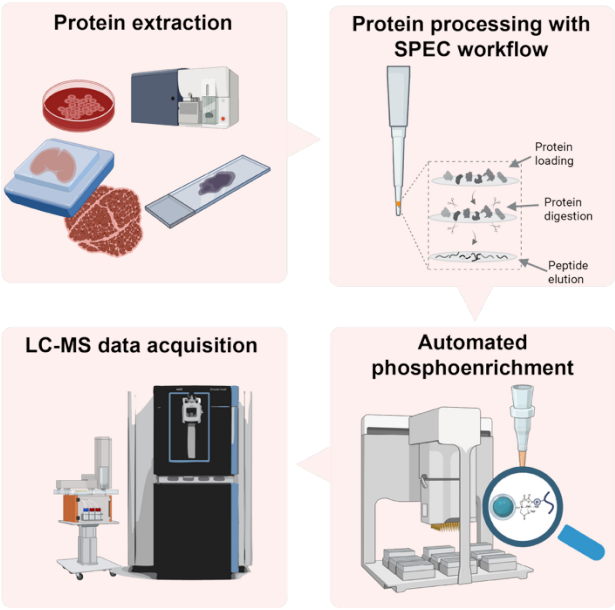

Figure 1 | Design of the nanoPhos workflow. Schematic overview of the nanoPhos platform for ultra-sensitive phosphoproteomics. The protocol enables efficient detergent-based lysis, proteolytic digestion, and peptide cleanup in nanoliter volumes. Zero dead-volume phosphopeptide enrichment eliminates absorptive loss of peptides and allows for streamlined injection of enriched phosphopeptides into LC-MS/MS.

We tuned the enrichment protocol for maximum selectivity and recovery, and eluted phosphopeptides directly into Evotips for seamless integration with downstream data-independent acquisition (DIA)-MS on an Orbitrap – Astral platform. The entire process, from cell or tissue lysate to MS-ready sample, is completed in under two hours and supports diverse input types, including primary material and archival tissue.

nanoPhos achieves orders of magnitude improvement in sensitivity

To evaluate the performance of nanoPhos and compare it to current state-of-the-art protocols, we set up an experimental workflow involving phosphopeptide enrichment from both bulk HeLa cell line lysates and FACS-sorted cells (**Fig. 2a**). For analysis of Orbitrap Astral phosphoproteome data we used directDIA in Spectronaut with standard settings (Methods). Starting with only 1 µg of input – at the low edge of literature reports – nanoPhos identified more than 55,000 unique phosphorylation sites, covering 4,900 protein groups, representing one of the deepest single-run phosphoproteomes reported to date (**Fig. 2b**). This only decreased by a third to 37,000 sites at 200 ng of input. Notably, we still obtained more than 8,000 sites at only 10 ng of which about 4,000 were Class 1 sites (localization probability > 75%) on 1512 proteins. Even in an unstimulated phosphoproteome of 55,000 phosphorylations we covered more than 60% of the 11,000 sites highly likely to be functional in a comparative bioinformatics study by the Beltrao group[19] ('functional score' > 0.5; **Suppl. Fig. 1a**).

To test how this remarkable sensitivity and depth transferred to individually selected cells, we generated a series of FACS-sorted samples, ranging from 3,000 to 100 HeLa cells. Our workflow allowed us to identify more than 20,000 unique phosphosites from 3,000 cells and about 9,000 sites from as little as 300 (**Fig. 2c**). Analysis of 100 sorted cells still yielded about 2,000 phosphorylation sites on 206 proteins, which notably included key factors such IRS2, GSK3B, and PRKCA (functional score > 0.5).

Importantly, increase in sensitivity is not compromised by quality of phosphopeptide enrichment. Across the whole dilution range, nanoPhos maintained a high median phosphopeptide selectivity of 82%, indicating minimal interference from unmodified peptides (**Fig. 2d**). We attribute this in part to a presence of 200 mM NaCl in the phosphopeptide enrichment buffer made possible by SPEC, which substantially reduces the portion of unmodified peptides (**Suppl. Fig. 2b**; Methods). To assess quantitative accuracy, we extracted linear regression curves for each phosphosite with at least three values across the dilution series and determined the overall coefficients of determination. The median of 0.94 for all phosphosites demonstrates high quantitative accuracy (**Fig. 2e**). Furthermore, triplicate inter-replicate measurements indicated excellent quantitative reproducibility with the median coefficient of variations of ~16% for dilution series and ~23% for FACS-sorted cells (**Suppl. Fig. 2c, d**).

Next, we directly compared our new nanoPhos workflow with the recently published µPhos

platform, using the Orbitrap Astral mass spectrometer for both protocols instead of the original timsTOF Ultra. The differences were most stark at 10 ng of input, where nanoPhos identified nearly one hundred times more phosphosites than µPhos. Between 100 ng and 1 µg, it still delivered a consistent five-fold increase (**Fig. 2f**). Of note, the set of phosphopeptides uniquely detected by nanoPhos was enriched for peptides with higher GRAVY indices, indicating increased detection of less accessible hydrophobic sequences (**Suppl. Fig 2e**).

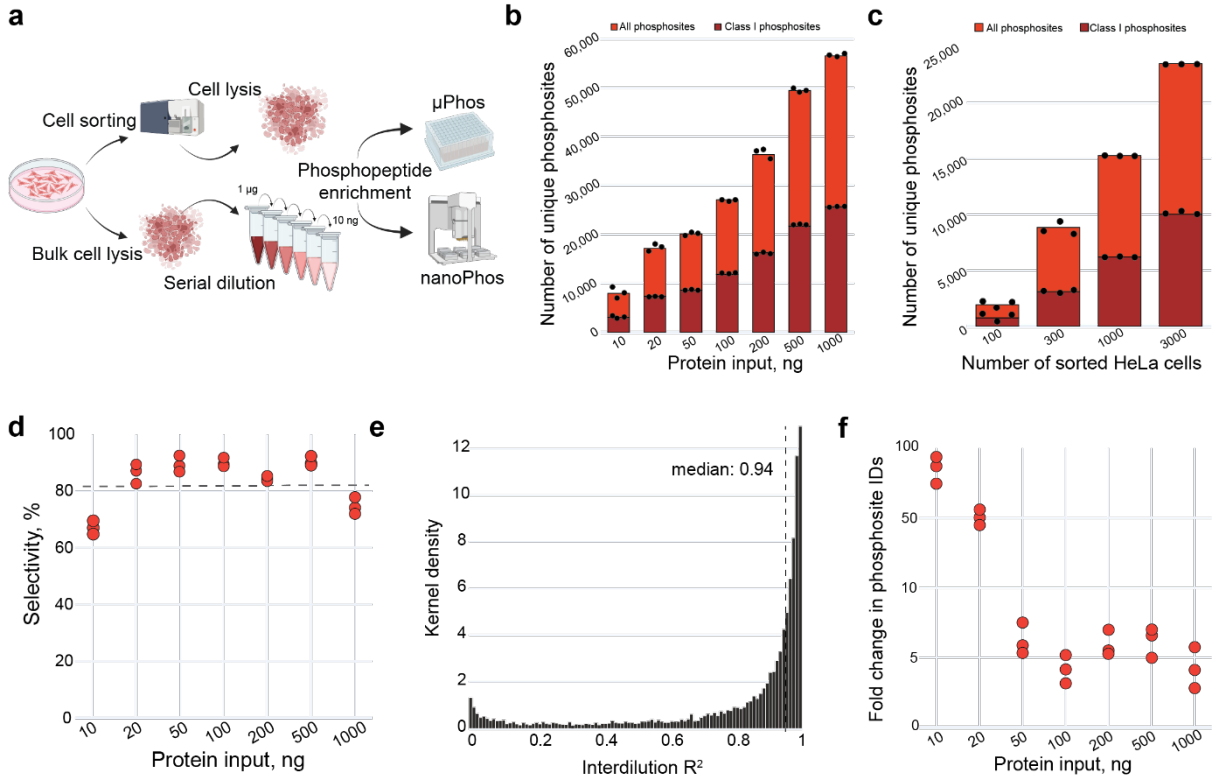

Figure 2 | Benchmarking nanoPhos sensitivity and quantitative performance. a, Experimental workflow overview. **b,** Number of identified phosphosites and Class I phosphosites (Spectronaut localization score > 0.75, darker color) as a function of input amount of HeLa cell lysate. **c,** Same as **b**, but for FACS-sorted HeLa cells. **d,** Selectivity of phosphopeptide enrichment in percent as a function of input amount of HeLa cell lysate. **e,** Coefficient of determination (R^2) for intensity of every identified phosphosite as a function of input amount of HeLa cell lysate. **f,** Fold change difference in phosphosite identifications between nanoPhos and µPhos across a dilution series of HeLa cell lysate.

nanoPhos captures phospho-signaling dynamics down to 10 ng input

EGF signaling in HeLa cells has been used for over 20 years as a prototypical cellular signaling system for evaluation of phosphoproteomics technologies[20–22]. Although this system is well-characterized, it remains a demanding test of quantitative fidelity, dynamic range, and biological interpretability, especially at low input levels. We treated HeLa cells with EGF for 15 minutes and performed a dilution series from 1 µg down to 10 ng of protein input prior to

phosphopeptide enrichment and nanoPhos analysis (**Fig. 3a**).

At 1 µg of starting material, we identified nearly 70,000 phosphosites, with approximately 8,700 showing significant regulation upon EGF treatment. The higher number of sites compared to unstimulated HeLa cells reflects the activation of this signaling pathway. Even the lowest input of 10 ng, yielded over 8,600 phosphosites, with 755 showing significant EGF-induced regulation using AlphaQuant's statistical engine[23] (**Fig. 3b**). For context, our recent optimized timsTOF workflow and a separate study employing fractionation on the Astral instrument each resulted in less than half the sites despite a hundred-fold more EGF-treated HeLa cells[21,22].

Canonical EGF-responsive phosphorylation sites—such as EGFR Y1194, MAPK1 Y187, FOXK1 S445, and SHC1 Y427—were robustly detected and upregulated across the entire dilution series, including the lowest input point, demonstrating not only the depth but also the biological coherence of nanoPhos-produced data (**Fig. 3c**).

Plotting all phosphosites with at least three quantified fold-change ratios across the dilution series, revealed that more than 90 % of them were in the 'low variability' range (CV < 0.5), including the canonical signaling sites (**Fig. 3d**). Top categories in a GO analysis of all the low-variability sites included EGFR-signaling, mTOR activation, ERK activation and S6K1 signaling (adj. p-values < 10^{-10} for all). Conversely, non-target 'Spliceosome' and 'Capped pre-mRNA processing' terms were enriched among high variability phosphosites. These categories were likely statistically significant because they contain a large number of annotated members, amplifying subtle effects that may only be indirectly related to the biological stimulus.

Pathway-level enrichment analysis confirmed biological coherence across all input amounts, with EGF-regulated cascades including MAPK and mTOR signaling showing consistent activation signatures down to 10 ng input (**Fig. 3e**).

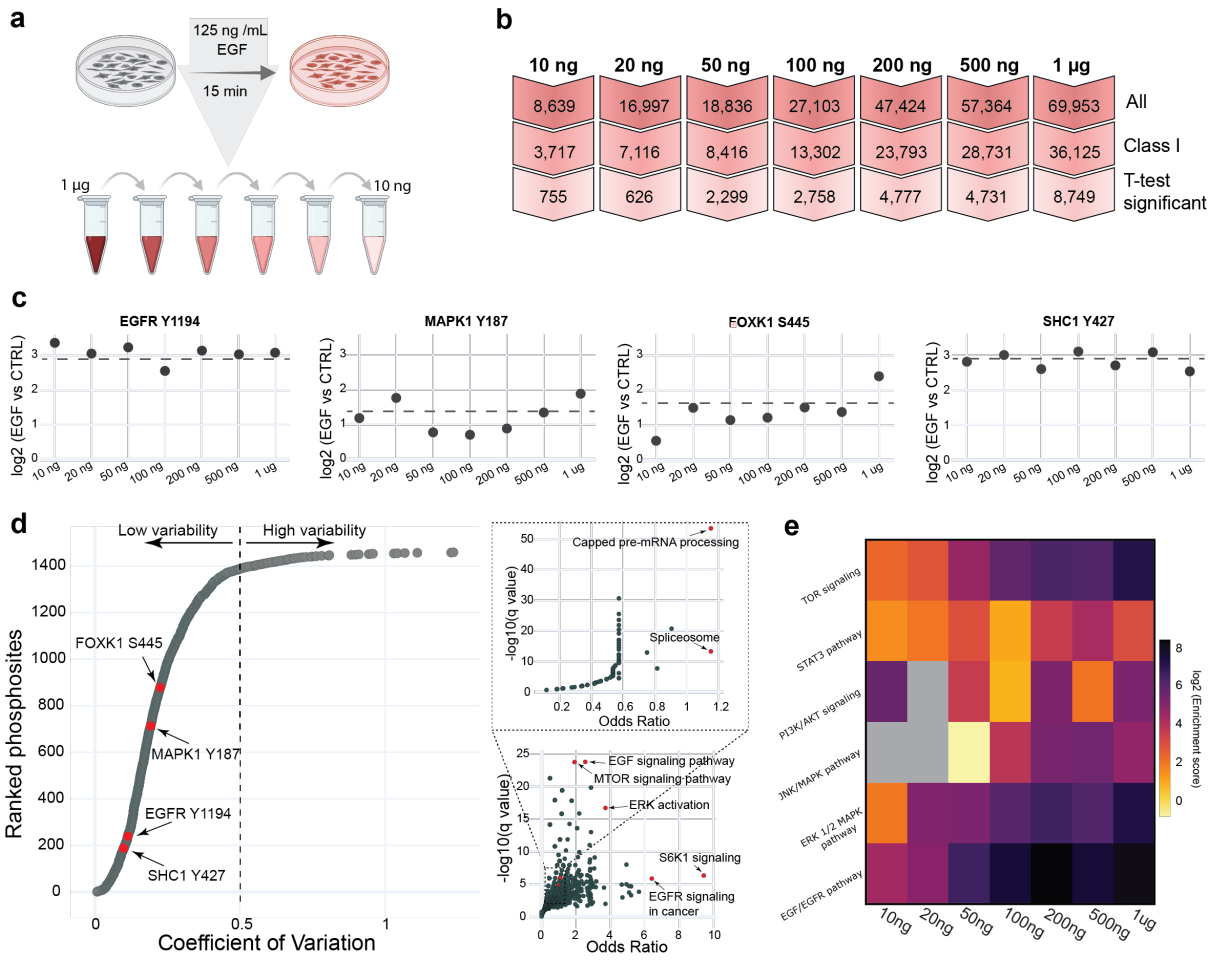

Figure 3 | Characterization of nanoPhos workflow in a biological setting. a Experiment schematics. **b** Number of unique, class I and t-test significant phosphosites across HeLa dilution series. **c** Intensity of selected canonical EGFR pathway-related phosphorylation sites as a function of HeLa protein input amount. **d** GO pathway enrichment analysis of main EGFR-related signaling pathways across a dilution series. **e** Inter-dilution variability of phosphosite fold changes (left panel). GO pathway enrichment analysis for low-variability (lower-right panel) and high-variability phosphosites (upper-right panel) using GOBP terms.

nanoPhos enables deep profiling of tissue phosphoproteome

Moving beyond cell lines, we next investigated the performance of our new workflow on fresh-frozen and formalin-fixed paraffin-embedded (FFPE) tissue. FFPE tissue is of particular interest because of the large number of samples stored in long-term biorepositories, but also poses challenges for tissue lysis due to the necessity of deparaffinization and removal of inter- and intra-protein cross-linking. This has typically confined phosphoproteome analysis to the hundreds of microgram range so far[24–26].

To investigate if our protocol can overcome these challenges, we prepared fresh-frozen and FFPE tissue from the same mouse brain, and diluted the lysate into 1 µg to 10 ng of starting protein material for nanoPhos (Methods). Notably, the presence of 2% SDC in our

standard nanoPhos protocol already fulfills the recommendations for FFPE[27], and therefore no specific changes needed to be implemented. With 1 µg of input, we identified about 40,000 unique phosphosites from fresh-frozen and about 20,000 from FFPE material (**Fig. 4a**). From 50 ng of starting protein material – the protein equivalent of just 50 motor neurons [28] – we identify more than 9,000 unique phosphosites from fresh-frozen and about 3,000 from FFPE tissue lysates. Median R^2 was 0.92 for fresh-frozen and 0.89 FFPE indicating high inter-dilution reproducibility (**Fig. 4b**).

Across the whole dilution series there was a consistent two to three-fold difference between the number of phosphosites identified in fresh-frozen and FFPE samples (**Suppl. Fig. 2a**). More than 80% of the FFPE phospho-proteome was contained in the fresh-frozen tissue phosphoproteome at both ends of the dilution series (**Fig. 4c-d**). While we did not observe marked differences in phosphorylated amino acid distribution between phosphopeptides found in fresh frozen and FFPE tissue, FFPE-specific peptides tended to be shorter and exhibited higher GRAVY indices, whereas multiply phosphorylated species were markedly underrepresented in FFPE samples (**Fig. 4e-f, Suppl. Fig. 2b-c**).

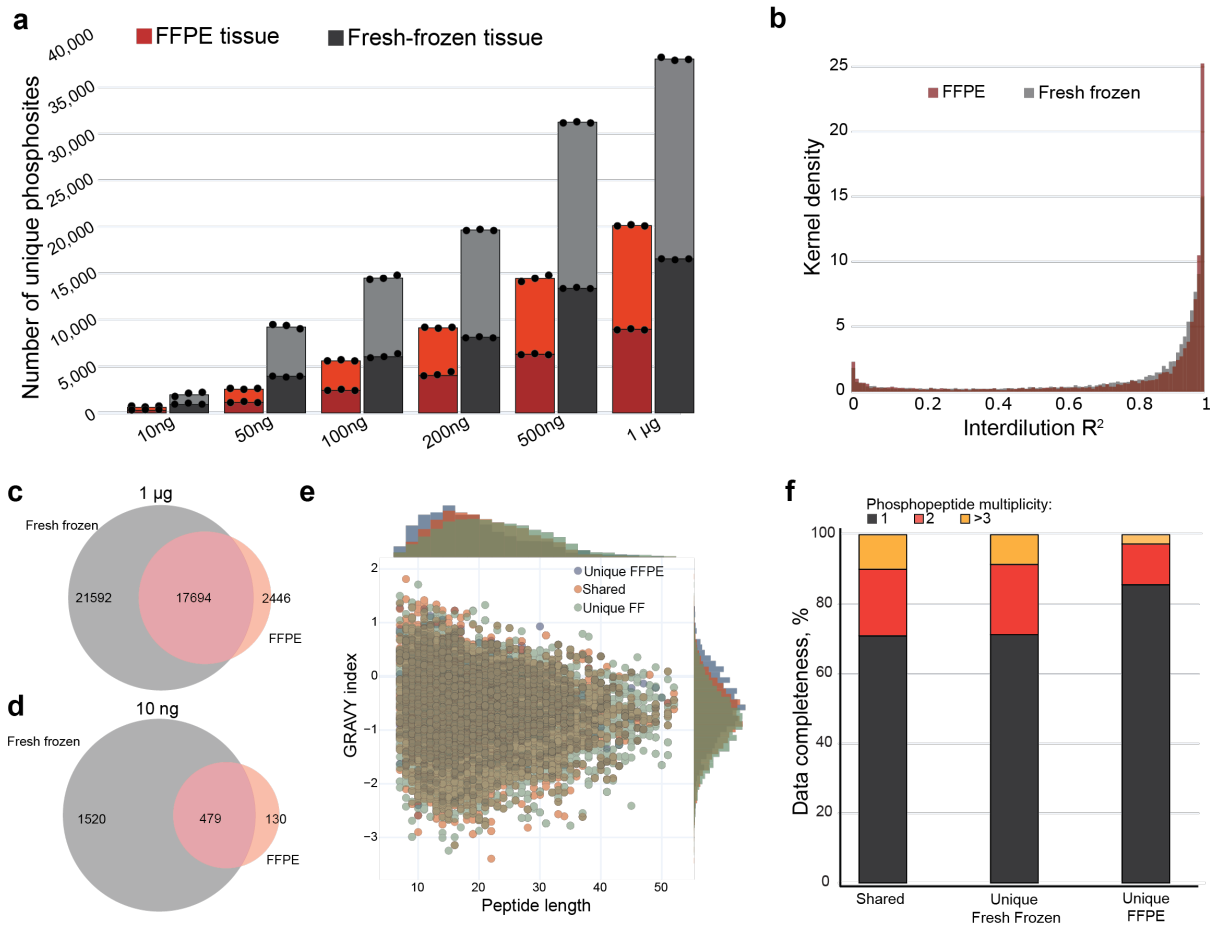

Figure 4 | nanoPhos enables deep phosphoproteomics from fresh-frozen and FFPE mouse brain tissue. (a) Number of unique and Class I phosphosites identified from fresh-frozen and FFPE mouse brain lysates across a dilution series from 1 µg to 10 ng input. **(b)** Quantitative reproducibility across inputs shown as R^2 values for phosphosite intensities. **(c)** Overlap of phosphosites identified in FFPE and fresh-frozen tissue at 1 µg protein input material. **(d)** Same as **(c)**, but for 10 ng starting protein material **(e)** Comparison of physicochemical properties between fresh-frozen and FFPE-specific phosphopeptides, including GRAVY index vs. peptide length. **f,** Percentage and multiply phosphorylated peptides in fresh-frozen and FFPE.

nanoPhos enables cell type-specific spatial phosphoproteomics

A long-standing aim in proteomics is to resolve functional signaling states in their native tissue context. This requires analyzing PTMs with cell-type and spatial specificity - a goal that has remained technically out of reach. We paired nanoPhos with DVP to obtain spatially resolved, cell type-specific phosphoproteomes from mouse brain tissue. Using high-content imaging, we first identified excitatory and inhibitory neurons within cortical and subcortical regions by multiplexed RNA-based fluorescence labeling of lineage markers (Slc17a7 and Satb2 for excitatory neurons; Gad1 and Gad2 for inhibitory neurons). Cell bodies were segmented and filtered by size, fluorescence intensities, and anatomic regions (Methods). Sampled neuron cells were individually laser microdissected from 10 µm thick, fresh-frozen, fixed brain

sections and collected into 384-well plates for nanoPhos processing (**Fig. 5a**; Methods).

We first assessed how many microdissected cellular contours ("shapes") were needed to reach meaningful phosphoproteomic depth. From only 100 shapes - representing roughly 40 neuron cell bodies - nanoPhos identified about 1,000 phosphosites. Increasing input to 1,500 shapes yielded more than 12,000 quantified sites, highlighting the ability of the workflow to reach classical phosphoproteome-scale depth from a small number of cells (**Fig. 5b**). We inspected the phosphopeptides corresponding to well-studied signaling events in the brain, including regulatory phosphorylation sites on phospho-tau, Syn1, Map2, and Camk2b. Their signal scaled linearly with the number of excised shapes and was clearly visible even at 100 shapes. Importantly, nanoPhos maintained high quantitative precision across the input range. Correlation analyses of fold changes across the shape dilution series revealed excellent reproducibility (R^2 ~0.92), mirroring results from sorted cells and bulk lysates (**Fig. 5c**). This deep coverage represents a spatially localized phosphoproteome at cellular resolution and shows that the full nanoPhos pipeline is compatible with tissue imaging, microdissection, and ultra-low input workflows, preserving both depth and quantitative accuracy.

To compare the phosphoproteomes of inhibitory and excitatory neurons within the cortex, we collected 1,000 excitatory and inhibitory neuronal shapes from cortical and subcortical mouse brain regions. This number of shapes represented the best trade-off between cutting time and phosphoproteome depth and is close to the 750 shapes that were the standard when DVP was introduced for global proteomics[14]. Additionally, from each region, we collected 100 shapes to complement phosphoproteomics analysis with the corresponding proteome dataset. This enabled us to normalize changes in the phosphoproteome to the underlying proteome (Methods). Together, we generated a dataset of more than 17,000 phosphorylation sites and 7,000 proteins (**Suppl. Fig. 3a, b**). We found high quantitative reproducibility among biological replicates for proteome and phosphoproteome datasets (**Fig. 5d, e and Suppl. Fig. 4c**). Interestingly, cell subtypes separated more clearly by the normalized phosphoproteomes than by the proteomes alone. Subcortical neurons showed increased phosphorylation in presynaptic proteins, as can be seen by the enriched terms associated with 'Synaptic vesicle exocytosis', 'Presynaptic membrane', and 'Regulation of synaptic vesicle cycle' (**Fig. 5g**; cluster A). Conversely, cortical neurons exhibited increased activity in terms related to postsynaptic density and assembly of postsynaptic structures (**Fig. 5g**; cluster D). Differential analysis of excitatory

and inhibitory neurons in the cortex revealed increased phosphorylation of 155 phosphosites on excitatory neurons, including sites on the well-known adapter protein Shank1, commonly associated with the post-synaptic density of excitatory neurons and widely expressed in cortical neurons, and 200 distinct phosphosites on inhibitory neurons. Furthermore, nanoPhos confirmed previously reported exhibition of postsynaptic upregulation of the NTRK1 signaling pathway in excitatory neurons[29] (**Suppl. Fig. 4d**).

These results establish that nanoPhos enables cell type–specific, spatially resolved phosphoproteomics in vivo, providing deep, quantitative insight into signaling heterogeneity across neuronal subtypes and brain regions.

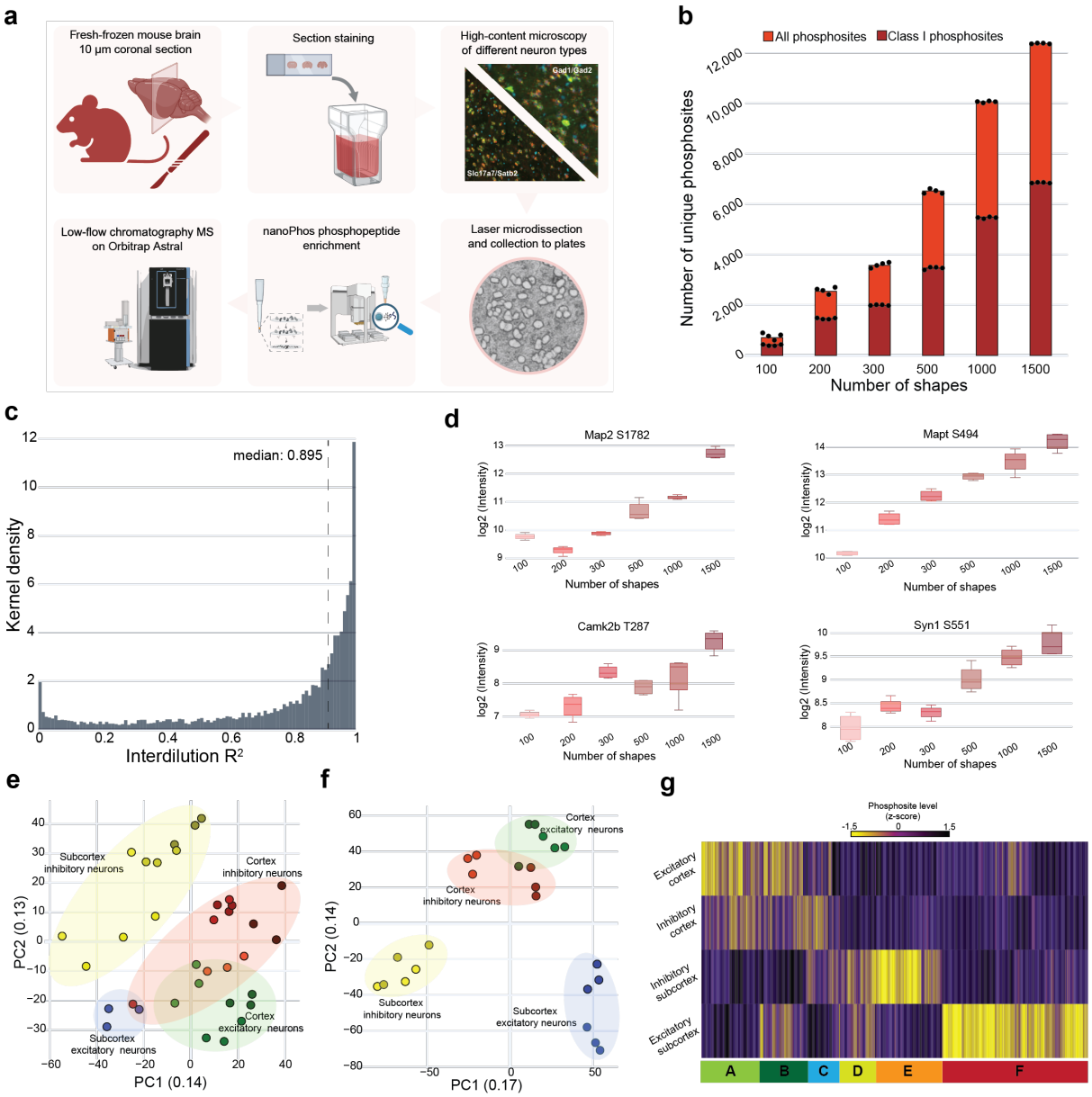

Figure 5 | Deep Visual Phosphoproteomics (phosphoDVP) of mouse brain reveals cell type– and region-specific signaling. (a) Schematic overview of Deep Visual Proteomics (DVP) applied to phosphoproteomics. **(b)** Phosphosite coverage as a function of the number of microdissected neuronal shapes. **(c)** Quantitative profiles of canonical phosphosites as a function of the number of excised shapes. (d) Quantitative reproducibility across shape input amounts shown as coefficient of determination. (e) PCA of the proteome and (f) PCA of the phosphoproteome for different spatially excised cell types. (g) Hierarchical clustering of ANOVA significant sites (FDR < 0.05).

Discussion

Here, we showed that nanoPhos overcomes key limitations of existing phosphoproteomics workflows by leveraging the SPEC protocol for high recovery sample preparation in nanoliter scale volumes, enabling deep, quantitative and robust phosphoproteomics from nanogram-scale protein inputs. Its design prioritizes compatibility with detergents, loss-less processing, and automation, which

are critical features for scarce or spatially defined samples. From HeLa lysate dilution series to sorted cells and tissue sections, we consistently achieve high phosphosite coverage, enrichment selectivity, and reproducible quantitation. At 10 ng input (corresponding to only 40 cells) the workflow accurately quantified key signaling sites and achieved a nearly hundred-fold higher coverage than the recent state-of-the-art µPhos workflow under the same MS conditions. Compared to our phosphoproteomics workflows of a decade ago, in which we generally required 10 mg of input material, nanoPhos on modern LC-MS instrumentation achieves a million-fold increase in sensitivity[30].

In FFPE tissue, despite challenges of crosslinking and embedding, nanoPhos recovered tens of thousands of phosphosites in the same standard workflow, with high overlap and reproducibility compared to fresh-frozen tissue, supporting retrospective analyses of clinical archives.

A "holy grail" of spatial biology is the *in vivo* measurement of the entire signaling state of an organism *in vivo* without mixing cell types. The most impactful advance may be the integration of nanoPhos with Deep Visual Proteomics (DVP), enabling the first global phosphoproteomic measurements in spatially and cell-type–resolved tissue contexts. phosphoDVP bridges molecular signaling and tissue architecture, a new dimension for understanding disease microenvironments and cellular heterogeneity *in vivo*.

The ability to measure phosphorylation events with spatial and cellular resolution opens new possibilities for functional tissue proteomics. In oncology, this could mean directly assessing the signaling state and vulnerability of different cancer cell populations to kinase inhibitors, quantifying signaling heterogeneity in immune infiltrates, or identifying drug-resistant clones within otherwise responsive lesions. In neuroscience, nanoPhos could help decode synapse-specific phosphorylation dynamics or capture drug-induced changes in different brain cell types and regions[10]. Combined with multiplexed imaging and AI-driven phenotyping, spatial proteomics will no longer be limited to static abundance, but include the dynamic regulation that defines cell state and fate.

Acknowledgements

We thank our colleagues at the Department of Proteomics and Signal Transduction at the Max Planck Institute of Biochemistry. In particular, we would like to thank Bianca Splettstößer and Igor Paron for technical support as well as Medini Steger for administrative support. We are grateful for FACS support by the Imaging Core Facility at

the Max Planck Institute of Biochemistry, in particular Martin Spitaler and Markus Oster.

Potential conflicts of interest

M.M. is an indirect shareholder in Evosep. All other authors declare no relevant conflicts of interest.

References

1. Mann, M. & Jensen, O. N. *Proteomic Analysis of Post-Translational Modifications*. http://www.nature.com/naturebiotechnology (2003).
2. Olsen, J. V. *et al.* Global, In Vivo, and Site-Specific Phosphorylation Dynamics in Signaling Networks. *Cell* **127**, 635–648 (2006).
3. Franciosa, G. *et al.* Proteomics of resistance to Notch1 inhibition in acute lymphoblastic leukemia reveals targetable kinase signatures. *Nat Commun* **12**, (2021).
4. Jayavelu, A. K. *et al.* The proteogenomic subtypes of acute myeloid leukemia. *Cancer Cell* **40**, 301-317.e12 (2022).
5. Kitata, R. B. *et al.* A data-independent acquisition-based global phosphoproteomics system enables deep profiling. *Nat Commun* **12**, (2021).
6. Humphrey, S. J., Azimifar, S. B. & Mann, M. High-throughput phosphoproteomics reveals in vivo insulin signaling dynamics. *Nat Biotechnol* **33**, 990–995 (2015).
7. Humphrey, S. J., Karayel, O., James, D. E. & Mann, M. High-throughput and high-sensitivity phosphoproteomics with the EasyPhos platform. *Nat Protoc* **13**, 1897–1916 (2018).
8. Needham, E. J. *et al.* Personalized phosphoproteomics identifies functional signaling. *Nat Biotechnol* **40**, 576–584 (2022).
9. Robles, M. S., Humphrey, S. J. & Mann, M. Phosphorylation Is a Central Mechanism for Circadian Control of Metabolism and Physiology. *Cell Metab* **25**, 118–127 (2017).
10. Liu, J. J. *et al.* In vivo brain GPCR signaling elucidated by phosphoproteomics. *Science (1979)* **360**, (2018).
11. Oliinyk, D. *et al.* µPhos: a scalable and sensitive platform for high-dimensional phosphoproteomics. *Mol Syst Biol* **20**, 972–995 (2024).
12. Zecha, J. *et al.* Decrypting drug actions and protein modifications by dose- and time-resolved proteomics. *Science (1979)* **380**, 93–101 (2023).
13. Bortel, P. *et al.* Systematic Optimization of Automated Phosphopeptide Enrichment for High-Sensitivity Phosphoproteomics. *Molecular and Cellular Proteomics* **23**, (2024).
14. Mund, A. *et al.* Deep Visual Proteomics defines single-cell identity and heterogeneity. *Nat Biotechnol* **40**, 1231–1240 (2022).
15. Rosenberger, F. A. *et al.* Spatial single-cell mass spectrometry

defines zonation of the hepatocyte proteome. *Nat Methods* **20**, 1530–1536 (2023).

16. Rosenberger, F. A. *et al.* Deep Visual Proteomics maps proteotoxicity in a genetic liver disease. *Nature* (2025) doi:10.1038/s41586-025-08885-4.

17. Kabatnik, S. *et al.* Deep visual proteomics reveals DNA replication stress as a hallmark of signet ring cell carcinoma. *NPJ Precis Oncol* **9**, 37 (2025).

18. Zheng, X., Mund, A. & Mann, M. Deciphering functional tumor-immune crosstalk through highly multiplexed imaging and deep visual proteomics. *Mol Cell* **85**, 1008-1023.e7 (2025).

19. Ochoa, D. *et al.* The functional landscape of the human phosphoproteome. *Nat Biotechnol* **38**, 365–373 (2020).

20. Bekker-Jensen, D. B. *et al.* Rapid and site-specific deep phosphoproteome profiling by data-independent acquisition without the need for spectral libraries. *Nat Commun* **11**, (2020).

21. Skowronek, P. *et al.* Rapid and in-depth coverage of the (phospho-)proteome with deep libraries and optimal window design for dia-PASEF. doi:10.1101/2022.05.31.494163.

22. Lancaster, N. M. *et al.* Fast and deep phosphoproteome analysis with the Orbitrap Astral mass spectrometer. *Nat Commun* **15**, (2024).

23. Ammar, C. *et al.* Tree-based quantification infers proteoform regulation in bottom-up proteomics data. Preprint at https://doi.org/10.1101/2025.03.06.641844 (2025).

24. Haines, M. *et al.* High-throughput proteomic and phosphoproteomic analysis of formalin-fixed paraffin-embedded tissue. Preprint at https://doi.org/10.1101/2024.11.17.624038 (2024).

25. Humphries, E. M., Loudon, C., Craft, G. E., Hains, P. G. & Robinson, P. J. Quantitative Comparison of Deparaffinization, Rehydration, and Extraction Methods for FFPE Tissue Proteomics and Phosphoproteomics. *Anal Chem* **96**, 13358–13370 (2024).

26. Friedrich, C. *et al.* Comprehensive micro-scaled proteome and phosphoproteome characterization of archived retrospective cancer repositories. *Nat Commun* **12**, (2021).

27. Humphries, E. M., Hains, P. G. & Robinson, P. J. Overlap of Formalin-Fixed Paraffin-Embedded and Fresh-Frozen Matched Tissues for Proteomics and Phosphoproteomics. *ACS Omega* (2025) doi:10.1021/acsomega.4c09289.

28. Rosenberger, F. A., Thielert, M. & Mann, M. Making single-cell proteomics biologically relevant. *Nature Methods* vol. 20 320–323 Preprint at https://doi.org/10.1038/s41592-023-01771-9 (2023).

29. Elmariah, S. B., Crumling, M. A., Parsons, T. D. & Balice-Gordon, R. J. Postsynaptic TrkB-Mediated Signaling Modulates Excitatory and Inhibitory Neurotransmitter Receptor Clustering at Hippocampal Synapses. *Journal of Neuroscience* **24**, 2380–2393 (2004).

30. Sharma, K. *et al.* Ultradeep Human Phosphoproteome Reveals a Distinct Regulatory Nature of Tyr and Ser/Thr-Based Signaling. *Cell Rep* **8**, 1583–1594 (2014).

31. Thielert, M. *et al.* Robust dimethyl-based multiplex-DIA doubles single-cell proteome depth via a reference channel. *Mol Syst Biol* **19**, (2023).

32. Tyanova, S. *et al.* The Perseus computational platform for comprehensive analysis of (prote)omics data. *Nature Methods* vol. 13 731–740 Preprint at https://doi.org/10.1038/nmeth.3901 (2016).

33. Chen, E. Y. *et al. Enrichr: Interactive and Collaborative HTML5 Gene List Enrichment Analysis Tool*. http://amp.pharm.mssm.edu/Enrichr . (2013).

34. Szklarczyk, D. *et al.* The STRING database in 2023: protein-protein association networks and functional enrichment analyses for any sequenced genome of interest. *Nucleic Acids Res* **51**, D638–D646 (2023).

Methods

Human cell culture

Human epithelial carcinoma cells of the line HeLa (ATCC, S3 subclone) were cultured in Dulbecco's modified Eagle's medium containing 20 mM glutamine, 10% fetal bovine serum, and 1% penicillin-streptomycin. Cells were routinely tested for mycoplasma contamination. For dilution series experiments, HeLa cells were cultured until 80% confluency, harvested with 0.25% trypsin/EDTA and collected in 15 mL falcon tubes. Cells were then washed twice with cold TBS and pelleted by centrifugation at 200*g* for 10 min. Next, supernatant was aspirated, cells were snap-frozen in liquid nitrogen and stored until further use. For EGF experiments, Hela cells at a plate confluence of 80% were treated for 15 min with 125 ng/mL animal-free recombinant human EGF or distilled water and washed three times with ice-cold TBS, snap-frozen in liquid nitrogen and stored in -80 °C until further use.

FACS sorting of HeLa cells

HeLa cells were cultured until 80% confluency, counted and harvested with 0.25% trypsin/EDTA to 15 mL falcon tubes. Cells were then washed twice with cold TBS, pelleted by centrifugation at 200*g* for 10 min and resuspended in TBS to achieve concentration of 1 million cells per 1 mL. Subsequently, 1 µL of DAPI was added to cell suspension and fluorescent-activated cell sorting (FACS) was performed on DAPI-negative live cell population. Cells were sorted into 384-well TwinTec Eppendorf plates containing 7 µL of lysis buffer (2% SDC, 0.1% DDM, 10 mM TCEP, 40 mM CAA in 100 mM Tris-HCl, pH 8.5), sealed with aluminum foil, centrifuged briefly and frozen at -80 °C until further use.

Mouse experiments

Eight-week-old female mice of genetic background C57BL/6J were used for excitatory and inhibitory neuron analysis. Animals used were bred for scientific purposes, and the research in this project does not involve experiments on animals (as defined by law). All animals were sacrificed by CO_2 euthanasia prior to removal of brains in accordance with the European Commission Recommendations for the euthanasia of experimental animals (Part 1 and Part 2). Breeding, housing, and euthanasia of the animals are fully compliant with all German (i.e., German Animal Welfare Act) and EU (i.e., Directive 2010/63/EU) applicable laws and regulations concerning care and use of laboratory animals.

Organ collection and immunofluorescence staining

After euthanasia, brains were dissected and embedded in Neg-50 (epredia). 10um coronal cryosections were collected onto 2um PEN

membrane slides (MicroDissect GmbH). Slides were stained with NucGreen (Thermo) 1:100 in PBS and HCR v3.0 probes to Slc17a7 and Satb2 (excitatory neurons) or Gad1 and Gad2 (inhibitory neurons) following the standard HCR v3.0 protocol (PMID: 29945988). HCR fluorescent amplifiers B2-546 and B4-647 were used for Slc17a7 and Satb2 probes, respectively, or for Gad1 and Gad2 probes, respectively.

High-content imaging and image processing

Imaging was performed on the Axioscan 7 slide scanner (Zeiss) equipped with Colibri 7 LED light source and appropriate filter sets (for 488, 546, and 647nm channels). A 20x NA 0.8 Plan-Apochromat objective was used. Z stacks were processed to single Z-planes with software Zen 3.7 (Zeiss) using the Extended Depth of Focus variance method, and then image tiles were stitched using the Zen stitching function. Stitched images were imported into Biological Image Analysis Software (BIAS, Single-Cell Technologies), and segmentation was carried out on the nuclear channel with Cellpose v2.3.2 and masks imported into BIAS. Brain images were hand-annotated for cortical vs sub-cortical regions, and double-positive cells (either for excitatory or inhibitory markers) from cortical vs sub-cortical regions were selected for laser microdissection.

Laser microdissection

Contour coordinates were imported, and shapes cut using the LMD7 (Leica) laser microdissection system in a semi-automated mode with the following settings: power 55; aperture 1; speed 75; middle pulse count 1; final pulse 0; head current 45 – 50%; pulse frequency 2.9 and offset 190. The microscope was operated with the LMD v8.5.9136 software, and samples collected into 384-well plates, leaving the outmost rows and columns empty. Plates were then sealed, centrifuged at 3,000*g* for 3 min, and frozen at -20 °C for further processing.

Cell lysis for cell culture experiments

For bulk cell lysate experiments, frozen HeLa cell pellets were resuspended in a lysis buffer (2% SDC, 0.1% DDM, 10 mM TCEP, 40 mM CAA in 100 mM Tris-HCl, pH 8.5) and boiled for 15 min at 95 °C while mixing at 1500 rpm, followed by high-energy tip sonication (10 pulses, 5 sec on, 5 sec off, 20% duty cycle). Lysates were then centrifuged for 5 min at max speed to remove cell debris. Protein concentration was determined via tryptophan assay. Sample was then diluted with 0.5% SDC in 100 mM Tris-HCl to the required input concentration and transferred to preequilibrated SPEC tips. For FACS-sorted cells experiments cell-containing 384-well plates were incubated for 15 min at 95 °C in a PCR cycler before loading on preequilibrated SPEC tips.

Tissue lysis for bulk dilution experiments

FFPE tissue samples were deparaffinized by incubating approximately 300 µg of sample in 300 µL n-Heptane for 1min at 30 °C and 700 rpm, discarding the solvent, repeating this step once more with n-Heptane, and two more times with 300 µl methanol. Deparaffinized FFPE and fresh-frozen tissues were resuspended in a lysis buffer and boiled for 5 min at 95 °C, followed by tip-sonication (10 pulses, 5 sec on, 5 sec off, 20% duty cycle). The samples were then boiled again for 5 min at 95 °C. Protein concentration was then determined using tryptophan fluorescence. Sample was then diluted with 0.5% SDC in 100 mM Tris-HCl to the required input concentration and transferred to preequilibrated SPEC tips.

Sample preparation of phosphoDVP samples

All liquid handling steps were performed on a Bravo pipetting robot as described previously[31]. During each incubation step plates were tightly sealed with two layers of aluminum foil to avoid evaporation. Shape-containing 384-well TwinTec Eppendorf plates were retrieved from the -20 °C and centrifuged at 3,000*g* for 2 min. The wells were then washed on the robot with 28 µl of 100% ACN and dried in a SpeedVac (Eppendorf) at 30 °C for 40 min. Shapes were then resuspended in 7 µl of lysis buffer and baked for 15 min at 95 °C in a PCR cycler at a lid temperature 110 °C. Plates were then centrifuged at 3,000*g* for 2 min and protein lysates were transferred to preequilibrated SPEC tips.

Sample preparation of DVP samples

All liquid handling steps were performed on a Bravo pipetting robot. Samples were collected into 384-well TwinTec Eppendorf plates and prepared via our standard DVP workflow[15]. Briefly, samples were lysed in 7 µl of 70mM TEAB and 0.013% DDM for 60 min at 95 °C. Next, 1 µL of 100% ACN was added to each well and plate next boiled for additional 60 min at 72 °C. Proteins were proteolyzed overnight with LysC and Trypsin at 37 °C in a PCR cycler. Resulting peptides were then acidified with 10% TFA and loaded onto preequilibrated EvoTips.

SPEC workflow

SPEC tips were prepared by placing two plugs of strong-anion-exchange (SAX) material (3M Empore) in a pipette tip with a blunt-ended syringe needle. Before sample loading, SPEC tips were activated with 50 µl 100% acetonitrile (ACN) and centrifugation at 700*g* for 1 min. Next, tips were preequilibrated with 50 µl SPEC Equilibration buffer (20 mM CAPS, 0.1% DDM in ddH_2O) and centrifuged at 700*g* for 3 min. Protein sample was then alkalinized by adding to equilibration buffer in ratio 1:10 and loaded on SAX material by centrifugation at 200*g* for 10 min. Proteins

were then on-tip digested by adding 5 µl of digestion buffer (0.25 µg/µl trypsin/LysC mix in 50 mM TEAB) and centrifuging for 20 sec at 100*g*. After digestion, peptides were eluted to 96-well TwinTec Eppendorf plate by addition of 20 µl elution buffer (1M NaCl, 0.1% DDM, 1% FA in ddH_2O).

Phosphopeptide enrichment

Peptides, eluted from SPEC digestion, were resuspended with 80 µl of phosphoenrichment buffer (90% ACN, 0.1% DDM, 1% FA in ddH_2O) to a final volume of 100 µl before phosphopeptide enrichment on the AssayMAP Bravo robot. Phosphopeptide enrichment cartridges, each containing 5 µl Fe(III)-nitrilotriacetic acid, were first primed with 100 µl priming buffer (1% FA, 99% ACN), followed by equilibration with 50 µl wash/equilibration buffer (1% FA, 80% ACN in ddH_2O). Peptides were then loaded on cartridges and subsequently washed with 50 µl wash/equilibration buffer. Phosphopeptides were eluted with 25 µl of elution buffer (500 mM $NH_4H_2PO_4$ in ddH_2O) directly onto preequilibrated EvoTips.

µPhos phosphopeptide enrichment

µPhos phosphopeptide enrichment was performed as described before[11]. Briefly, HeLa protein lysates were transferred to 96-well deep-well plates (Eppendorf) and diluted with the lysis buffer to 19 µl. 1 µl of digestion buffer was added to each well. Plate was then sealed with a silicone mat and incubated for 2 hours at 1,500 rpm at 37 °C. After digestion, plate was briefly centrifuged and 20 µl of 100% 2-propanol was added and plate was incubated for 30 sec at 1,500 rpm, followed by addition of 40 µl of µPhos Enrichment Buffer. Next, 5 µl of 1 mg/µl TiO_2 solution was added to peptides, after which plate was incubated at 40 °C at 1,500 rpm for 7 min. Plate was then centrifuges and supernatant was aspirated with a multi-channel pipette. Beads were then washed five times with 200 µl of µPhos Washing Buffer. Next, beads were transferred to C8 StageTips and centrifuged at 700*g* for 7 min. Phosphopeptides were then eluted by two-step addition of 30 µl of µPhos Elution Buffer and centrifugation for 4 min at 700*g*. Eluated were then vacuum dried for 30 min at 45 °C until <10 µl was left. 200 µl of Evosep buffer A (0.1% FA in ddH_2O) was then added to eluates and solution was transferred on preequilibrated EvoTips.

Peptide loading of C-18 tips

C-18 tips (Evotip Pure, Evosep) were washed once with 50 µl of buffer B (99.9% ACN, 0.1% FA), activated for 1 min in 2-propanol and equilibrated with 50 µl of buffer A. Phosphopeptides were then eluted into 225 µl of buffer A in the tip, which was then centrifuged for a few seconds. After peptide binding, the disk was further washed once with 75 µl buffer A and further overlayed with 150 µl buffer A. All centrifugation steps were

performed at 700*g* for 1 min, except sample loading for 2 min.

LC-MS/MS analysis

The samples were analyzed using an Evosep One LC system (Evosep) couple to an Orbitrap Astral Zoom mass spectrometer (Thermo Fisher Scientific). Peptides were eluted from the Evotips using a 'Whisper Zoom' gradient with a throughput of 80 samples per day on an Aurora Rapid column of 5-cm length, 75-µm-internal diameter, packed with 1.7 µm C18 beads (IonOpticks). The column temperature was maintained at 60C using a column heater (IonOpticks). The Orbitrap Astral Zoom was equipped with an EASY-Spray source (Thermo Fisher Scientific). An electrospray voltage of 1,900 V was applied for ionization, and the radio frequency level was set to 40. Orbitrap MS1 spectra were acquired from 380 to 1,380 m/z at a resolution of 240,000 (at m/z 200) with a normalized automated gain control (AGC) target at 500% and a maximum injection time of 3 ms. For the Astral MS/MS scans in data-independent acquisition (DIA) mode, we used 100 variable isolation windows, designed with a pyDIAid software[21]. A maximum injection time of 10 ms was used. The isolated ions were fragmented using high-energy collisional dissociation with 25% normalized collision energy.

Spectral search

LC-MS raw files were processed in Spectronaut v19.9 without experimental spectrum libraries ('directDIA+' workflow in Spectronaut). Data were searched against the UniProt human or mouse reference proteome (accessed August 2024). We set the protease specificity to trypsin with a maximum number of two missed cleavages and required a minimum peptide length of 7 amino acids. The mass tolerances for precursor and fragment ions were set to 'Dynamic' for both MS1 and MS2 level. False discovery rates were controlled by a target-decoy approach to ≤1% at precursor and protein levels. For phosphoproteomics experiments, we defined cysteine carbamidomethylation as a fixed modification and protein N-terminal acetylation, methionine oxidation and serine/threonine/tyrosine (STY) phosphorylation as variable modifications in 'BGS Phospho PTM Workflow' and activated the PTM localization mode. For proteomics runs we used 'BGS Factory Settings (default)' workflow with default settings. To report all identified phosphopeptides, we defined a localization probability score threshold of 0 and, if applicable, filtered the output on the phosphosite level as described below. Quantification values were filtered by q-value and we defined the 'Automatic' normalization mode for cross-run normalization.

Data analysis

All data processing and analysis steps were performed in the Python programming environment (v.3.13). We exported tabular data in the Spectronaut 'BGS Factory Report' scheme with 'EG.PrecursorID', 'PEP.PeptidePosition', 'EG.PTMAssayProbability', 'PG.Genes' and 'PG.ProteinGroups' as additional columns and parsed the output with a custom Python implementation of the 'PeptideCollapse' plugin for Perseus[32]. Reverse sequences, common contaminants, phosphosites with localization probability < 0.75 and phosphosites quantified in <70% of technical/biological replicates were removed and remaining missing values were imputed by random sampling from a downshifted normal distribution as previously described, Two-way ANOVA, unsupervised hierarchical clustering and PCA were performed in Python using scripts adapted from the Clinical Knowledge Graph analytics core. Pathway enrichment analysis was performed using an EnrichR software and String database[33,34]. Volcano plot analysis and proteome-based normalization of phosphoproteome data were performed with the AlphaQuant python package[23].

Supplementary Figures

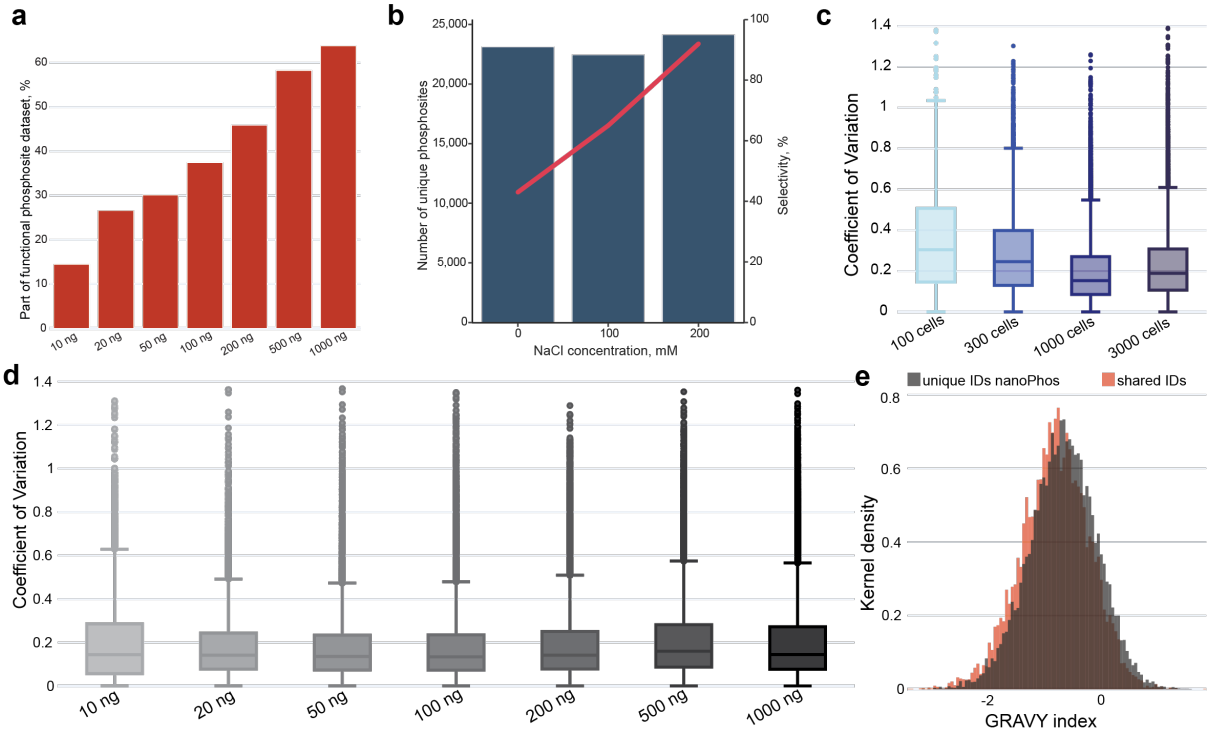

Supplementary Figure 1. a Percentage of functional phosphosite dataset (functional score > 0.5) identified in dilution series experiment. **b** Number of unique phosphorylation sites and selectivity (secondary y-axis) as function of NaCl concentration in the phosphoenrichment buffer. **c** Precision of label-free phosphopeptide quantification in workflow replicates ($n = 3$) for the conditions in Fig. 2C. The box depicts the interquartile range with the central band representing the median value of the dataset. The whiskers represent the furthest datapoint within 1.5 times the interquartile range. Points indicate outliers. **d** Same as **c** but for HeLa lysate dilution series. **e** Overlay of the GRAVY hydrophobicity index of phosphopeptides, unique to nanoPhos and IDs, shared in nanoPhos and µPhos ($n = 3$).

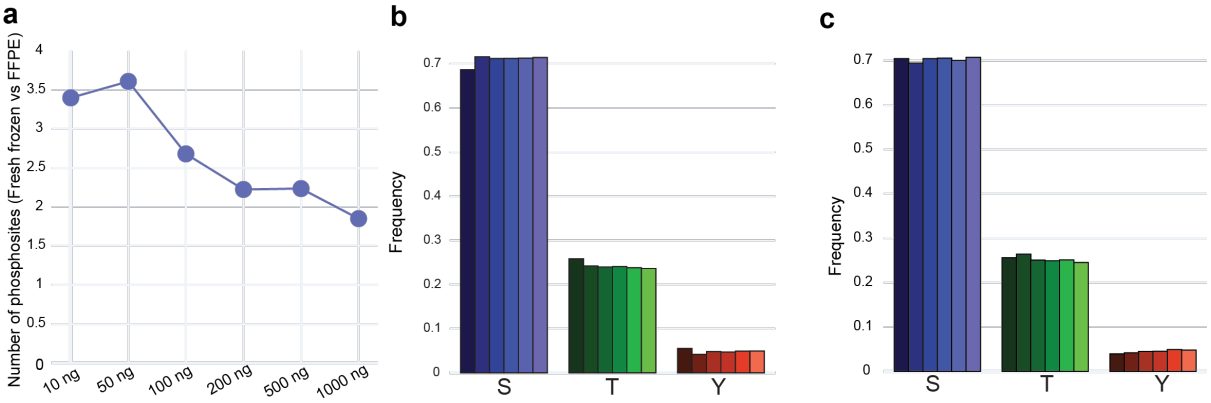

Supplementary Figure 2. a Fold change difference in phosphosite identifications between fresh-frozen and FFPE tissue as a function of tissue protein input. **b** Relative number of phosphorylated serine, threonine, and tyrosine sites in fresh-frozen tissue dilution series. **c** Same as **b**, but for FFPE tissue dilution series.

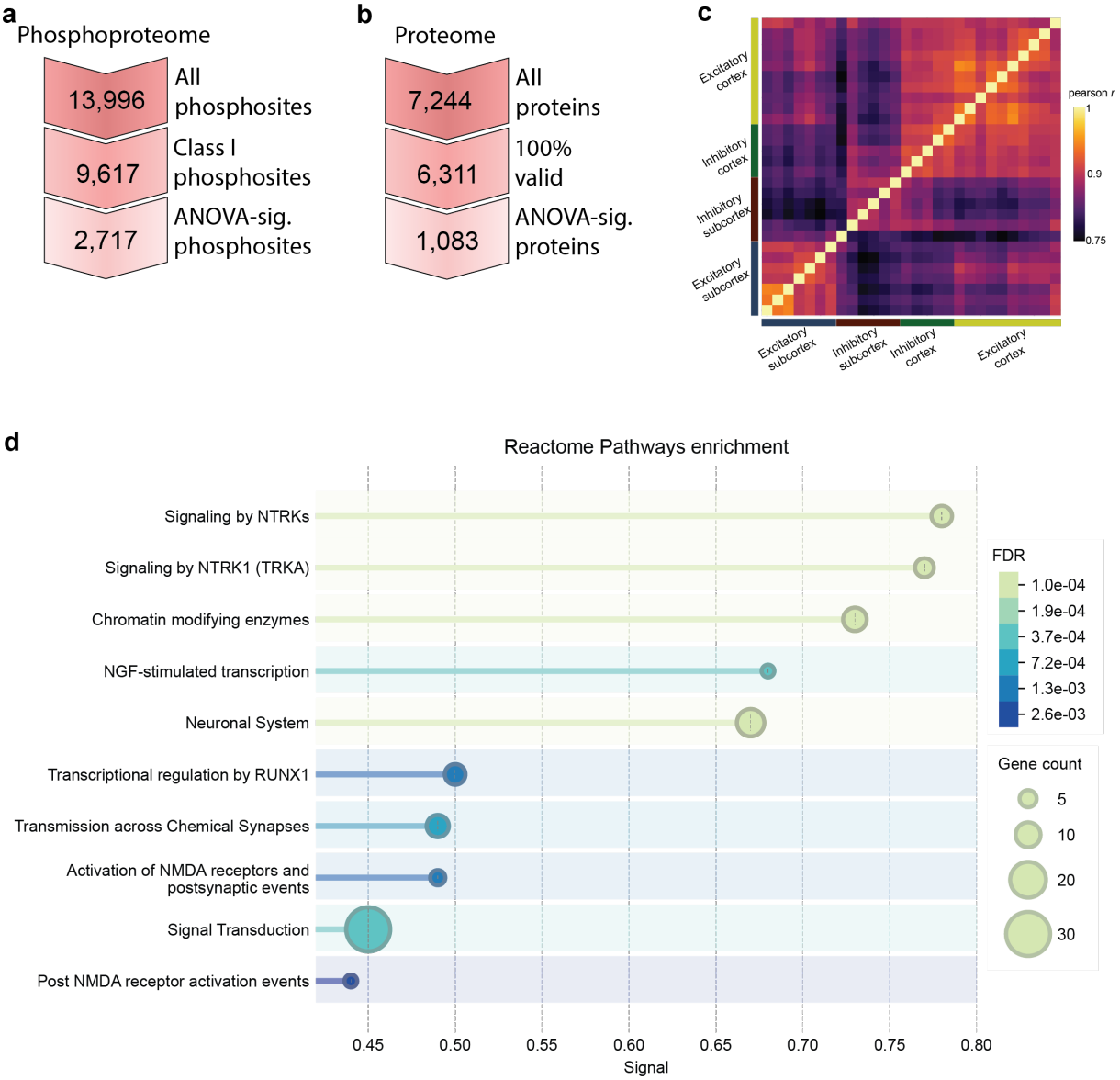

Supplementary Figure 3. a Number of unique phosphosites, class I phosphosites and ANOVA-significant phosphosites, identified in the mouse brain pDVP experiment. **b** Number of protein groups, protein groups identified with 100% data completeness and ANOVA-significant protein groups, idenitified in the mouse brain pDVP experiment. **c** Pairwise Pearson correlation analysis of all phosphoproteomics samples. **d** Reactome pathways enrichment of phosphorylated proteins, upregulated in excitatory cortical neurons as opposed to cortical inhibitory neurons. Plot adapted from String database.